QUANTIFYING FATIGUE FAILURE USING THE POWER DENSITY THEORY

A Thesis

by

ZACHARY THOMAS BRANIGAN

Submitted to the Office of Graduate and Professional Studies of
Texas A&M University
in partial fulfillment of the requirements for the degree of

MASTER OF SCIENCE

Chair of Committee,	C. Steve Suh
Committee Members,	Gary Fry
	Harry Hogan
Head of Department,	Andreas Polycarpou

August 2016

Major Subject: Mechanical Engineering

ABSTRACT

Fatigue is the most common mechanical cause of engineering failures, but it is not well understood. Current methods of predicting fatigue failure rely on empirically-derived equations instead of having a truly scientific foundation. These have very high uncertainties, and they often do not consider the cycling frequency even though it has been proven to affect fatigue life. The power density theory is a new way of describing fatigue. It is based on the concept of power density, which is physically equivalent to the amount of power deposited into a unit volume. Power density results from changes in stress magnitude over time. Stress alternations that occur across a broad bandwidth of frequencies must be factored in. Higher frequencies coupled with faster changes in stress contribute more power density. Power density accumulates at every frequency and time, damaging the part. After this accumulation reaches the material's power density threshold, a fundamental property of the material, it is expected to fail by fatigue.

A previously-published multiaxial vibration fatigue test was referenced and replicated using computer simulations, and the concept of power density was applied to predict its results. This served as a feasibility study for the theory, as well as an example of how to apply it. The power density response of the system was analyzed, and the failure locations were predicted for each of the ten load cases considered. The predicted failure locations followed the same trend as the experimental results. These results were promising, so more research is recommended to further test and develop the power density theory. Further examination of the theory could result in a better understanding of fatigue failure, improving engineering work across many industries.

TABLE OF CONTENTS

Page

LIST OF FIGURES

Page

LIST OF TABLES

Page

CHAPTER I
INTRODUCTION

I.1 Fatigue Failure

The stresses in components often vary over time. A specimen can crack after enough repeated stress fluctuations even if the stresses remain well below the material's ultimate strength. This is known as fatigue failure. Unlike static failures, which usually yield before completely failing, fatigue failures generally occur suddenly with very little perceptible warning. Additionally, there is currently no reliable, scientific way to predict how long a part will last under alternating stresses. As a result, the majority of mechanical engineering failures occur in this manner.

Fatigue failure is caused by fluctuating plastic deformation, often on a microscopic level. This can occur even when the main body of a part behaves elastically [1]. Repeated local yielding can cause microcracks to form by crystallographic propagation. The microcracks decrease local ductility and create small stress concentrations. After these cracks are initiated, continued stress alternations cause them to propagate incrementally, forming visible macrocracks. Eventually, the cracks reach a critical size where the remaining material can no longer support the loads. The part then fractures suddenly [2,3].

The number of stress cycles that occur before these cracks initiate and propagate has been proven to depend on the frequency at which the alternations occur [4,5,6,7]. Higher cycling frequencies typically cause cracking and failure after fewer cycles than lower-frequency fluctuation. However, this trend is not accounted for in most fatigue calculations.

I.2 Methods of Predicting Fatigue Failure

One of the most commonly used methods of predicting fatigue failure is the stress-life method [3]. It is based on the concept that every material has a fatigue strength related to the number of stress alternations that it experiences. After a specimen

experiences a certain number of alternations at the corresponding fatigue strength, it is expected to fail. The fatigue strength (S'_f) after N number of cycles is estimated using the following equation:

$$\left(S'_f\right)_N = \sigma'_F(2N)^b \tag{1}$$

where σ'_F is the true stress experienced by the part and often needs to be approximated. The coefficient b is calculated as follows:

$$b = -\frac{\log\left(\frac{\sigma'_F}{S_e}\right)}{\log(2N_e)} \tag{2}$$

where S_e is the endurance limit and N_e is the endurance limit's corresponding cycles to failure. The endurance limit is the lowest stress at which fatigue failure would be expected after a very large number of cycles. It is estimated using the following equation:

$$S_e = k_a k_b k_c k_d k_e k_f S'_e \tag{3}$$

where S'_e is the endurance limit of an idealized test specimen. The k factors modify the equation depending on the part's surface condition and size, the stress levels and temperatures it experience, and miscellaneous other factors. Each k factor is estimated empirically, usually using multiple empirically-determined constants and curve fits.

The stress-life method has many obvious issues. There is no proper scientific basis for most of the values and equations that are used. Instead, it relies on empirical equations and probabilities based on many variables. Many values with high uncertainties are combined, causing the potential error to compound. Additionally, it is based on static properties despite the fact that fatigue is a dynamic event. It neglects the cycling frequency even though it has a proven effect on a part's lifetime. All time-domain methods of predicting fatigue failure have this problem. Many newer fatigue calculations still utilize the stress-life relationship between the fatigue strength and its corresponding number of cycles to failure. Thus, these newer methods inherit many of the issues inherent in the stress-life method.

The strain-life method [3] has shown to be more accurate than the stress-life method. It uses the strain amplitude at the local discontinuity that eventually fails to

estimate the relationship between the strain amplitude and the number of cycles to failure. It utilizes the Manson-Coffin relationship to estimate the total-strain amplitude $\left(\frac{\Delta\varepsilon}{2}\right)$ at which the part is expected to fail after *N* number of cycles:

$$\frac{\Delta\varepsilon}{2} = \frac{\sigma_F'}{E}(2N)^b + \varepsilon_F'(2N)^c \tag{4}$$

where *E* is the modulus of elasticity and *b* and *c* are constants that fit the strain-life curve to empirical data. σ'_F and ε'_F are the true stress and strain experienced by the failure location that correspond to fracture after one cycle. This relationship is used to predict the fatigue damage and eventually failure of a specimen.

Strain-life's usefulness is limited by the lack of "strain concentration" information for determining the total strain at a discontinuity. It also uses compounding idealizations, resulting in high uncertainty [3]. Like in the stress-life method, cycling frequency is not considered at all. Despite these issues, strain-life concepts are often used in newer methods of predicting fatigue failure.

More recently, frequency-domain methods of determining fatigue damage have been examined. The Dirlik method [8,9] combines one exponential and two Rayleigh probability densities to approximate the cycle-amplitude distribution (p_a) from the stress using the following equation:

$$p_a(s) = \frac{1}{\sqrt{m_0}}\left[\frac{G_1}{Q}e^{-\frac{Z}{Q}} + \frac{G_2 Z}{R^2}e^{-\frac{z^2}{2R^2}} + G_3 Z e^{-\frac{z^2}{2}}\right] \tag{5}$$

where *Z* is the normalized amplitude, x_m is the mean frequency, and the other parameters depend on the mean frequency and the spectral width as described by Dirlik [9]. The fatigue-life intensity $\overline{D}^{DK}$ is calculated by Dirlik using the following equation:

$$\overline{D}^{DK} = C^{-1} v_p m_0^{\frac{k}{2}}\left[G_1 Q^k \Gamma(1+k) + \left(\sqrt{2}\right)^k \Gamma\left(1+\frac{k}{2}\right)(G_2|R|^k + G_3)\right] \tag{6}$$

where the parameters are described by Dirlik. This method is considered one of the most accurate frequency-domain methods for predicting fatigue failure. However, it still can have very large error for some cases [8]. It is also based on probabilities found from numerical simulations instead of having a proper scientific basis.

Another frequency-domain approach is the Tovo-Benasciutti method [8,10]. This method estimates fatigue life by linearly combining upper and lower fatigue-damage intensity limits. The intensity of fatigue damage ($\overline{D}^{TB}$) is then calculated using the following equation:

$$\overline{D}^{TB} = [b + (1 - b)\alpha_2^{k-1}]\alpha_2 \overline{D}^{NB} \quad (7)$$

where b is approximated using numerical simulation data, α_2 and α_2^{k-1} are spectral width parameters, and $\overline{D}^{NB}$ is the narrow-band damage intensity. This method has been found to be accurate under certain conditions [8]. Like the Dirlik method, though, it is a primarily numerical estimation instead of being based on true theory. It is not always able to predict fatigue lifetimes well. Additionally, frequency-domain methods do not appropriately consider the time domain, limiting their ability to fully capture the system response when the frequency response is not constant at all times.

In 2008, Abdullah et al. [11] attempted to use the time-frequency domain in fatigue analysis. They based their analysis on fatigue strain data. They used the concept of power spectral density (PSD) to take this data from the time domain and determine its power in the frequency domain. PSD is denoted by S_{xx} and calculated using

$$S_{xx}(\omega) = \lim_{T\to\infty} E[|\hat{x}_T(\omega)|^2] \quad (8)$$

where T is the time interval being examined, $\hat{x}_T$ is the Fourier transform of the signal, and E is the expected value [12]. Instead of doing this for the entire time interval, though, Abdullah et al. used the short-time Fourier transform (STFT) method to give the PSD at different time intervals. The resulting strain intensities were then used to determine the damage on the part due to each frequency at each time. This damage was considered relative to the expected strain life of the material (from the Manson-Coffin relationship, Equation 4) to estimate its fatigue life. There are multiple problems with this strategy. Because it uses the strain-life method to predict the number of cycles to failure, it inherits the uncertainty in that relationship. Even though the strains were separated by the frequencies at which they occurred, no discrepancy was made to account for the differences in fatigue damage from low frequencies versus high frequencies. The Manson-Coffin relationship is intended for use in the time domain.

Also, the STFT simply applies a Fourier transform to time intervals separately. The resulting values would be poorly localized in the time-frequency domain per the Uncertainty Principle, which is discussed in Chapter II.

I.3 Time-Frequency Analysis

Signal oscillation over time can occur at multiple frequencies simultaneously. It is impossible to determine all of the frequencies that contribute to the total signal at every time using a time-domain representation of the signal. The changes in stress due to each frequency are combined at every time interval, and all frequency information is lost. Meanwhile, frequency-domain representations of a signal – such as Fourier transforms [13] – are unable to discern the times at which oscillations occur at each frequency. For example, they would not see any difference among a signal that occurs at a low frequency before switching to a high frequency, a signal that occurs at the same high frequency before switching to the same low frequency, and a signal that occurs at both frequencies simultaneously. It is only by viewing the signal in the time-frequency domain that its full properties can be resolved.

A complete fatigue theory must account for the cycling in both the time and frequency domains. There are many methods of making the transformation from the time domain to the time-frequency domain. These need to be considered, and the best one for this application should be chosen. This is discussed in more detail in Chapter II.

I.4 Finite Element Analysis

Complex equations are usually required to define the properties and reactions in continuous bodies. If such equations even exist, they often require high-order calculations and differential equations. The difficulty of these calculations, along with the computation time needed to perform them, make it impractical to use continuum methods in most cases. The finite element method is a useful tool for simplifying many engineering problems.

In finite element modeling, bodies are discretized into an equivalent system of many smaller bodies. A system of simultaneous algebraic equations can then be solved to approximate the properties at a finite number of points on a body. These equations are often simplified to significantly streamline the required calculations. If the body is discretized into enough finite elements, this method can give very accurate results while requiring relatively little computation time and effort [14]. In addition, many commercially-available computer programs exist that assist with finite element analysis.

The Abaqus finite element analysis software was used for this research. Abaqus is a highly versatile program that is capable of reliably and efficiently performing advanced finite element calculations. The Abaqus/Explicit analyzer was used to process the simulations. Abaqus/Explicit is based on the forward Euler algorithm, which is a mathematical method for integrating the equations of motion through time [15]. The integration time step is adaptive in time. This method is only conditionally stable, depending on the stability limit. It uses a lumped mass matrix *M* to calculate the nodal accelerations $\ddot{u}$ at any time *t'* using the following equation:

$$\ddot{u}(t') = M(t')^{-1}[P(t') - I(t')] \tag{9}$$

where *P* is the external load vector and *I* is the internal load vector. This integration scheme is optimized for nonlinear systems and transient loads [16]. Abaqus/Explicit was chosen for this research so that the transient stress waves across a broad bandwidth of frequencies could be well-captured.

I.5 Research Objectives

Current fatigue methods can be successfully applied to some situations, but they are incomplete. A new way of viewing fatigue failure is necessary to more fully understand it. It should be less reliant on empirical or numerical data and instead have its foundation in proper scientific theory. Both the time and frequency domains must be considered to completely describe the response of the system. The primary objective of this research was to explore a scientifically-based method of predicting and explaining fatigue failure using time-frequency analysis.

The power density theory was developed to satisfy these objectives. This theory is based on the real physical phenomenon of stress alternations, which are physically equivalent to depositing power into a volume. This process damages a material. Stress fluctuations cause more damage when they occur at higher frequencies. In order to determine the magnitude of the changes in stress that occur at each time and frequency, these changes are transformed into the time-frequency domain. The damage is then scaled based on both the changes in stress and their corresponding frequencies.

The research focused on developing the power density theory. A feasibility study was then performed with computer simulations that recreated previous physical testing. These simulations were executed using the Abaqus/Explicit program. The data from the simulations was processed with a MATLAB program that used the power density theory to predict fatigue failure. This served as an example for how the power density theory can be applied to a real problem. The power density results were compared to the experimental results as a test of the theory's viability. Additionally, future research on the power density theory and the potential applications of it were considered.

Some assumptions were required for the feasibility study. Because some dimensions of the previous testing were not known, these dimensions were estimated based on images of the experimental setup. Additionally, vibration excitations that were applied during testing were approximated in Abaqus as sinusoidal waves at the peak measured frequency. The amount of data that could be output was limited by the computer memory. Therefore, the simulations were not run until predicted failure. Instead, they completed shortly after the system reached a consistent response. This response was assumed to continue until the part failed. Power density calculations were only performed on the surface where the cracking occurred during physical testing, and the sampling frequency was limited. Both of these measures were taken to reduce the required computer memory.

CHAPTER II
TIME-FREQUENCY ANALYSIS

II.1 Time-Frequency Analysis

Proper time-frequency analysis can be used to transform a signal from the time domain to the time-frequency domain. It can resolve the contributions of each frequency to the total signal at each time. Taking a cross-section of the signal's time-frequency representation at a single time should show how much each frequency contributes to the signal at that time. Similarly, taking the cross-section of a signal's time-frequency representation at a single frequency should show how much that frequency contributes to the signal at each time.

The following three properties must be satisfied for a time-frequency analysis to be valid [17]. First, the transformed values at each time and frequency must be real, and integrating them over all times and frequencies must result in the total signal energy. This is represented in the following equation:

$$\int_{-\infty}^{\infty}\int_{-\infty}^{\infty}\rho_z(t,f)\,dt\,df = E_z \tag{10}$$

where ρ_z is the transformed signal energy at time t and frequency f and E_z is the total signal energy. Second, Equation 10 must also be true when only considering any given region of times and frequencies. Third, at any time, all peak values of the transformed signal must occur at the same frequency as the local maximum frequencies at that time. This ensures that the time-frequency localization is correct and that the signal's components are being attributed to the appropriate times and frequencies.

One major limitation in time-frequency analysis is the Uncertainty Principle. In time-frequency analysis, the Uncertainty Principle [18] dictates that there is a limit to the precision at which both time and frequency can be known. Good time localization yields poor frequency localization, and good frequency localization yields poor time localization. For any application, the optimal balance of time and frequency localization must be chosen. Better time resolution is required for high frequencies while better frequency resolution is preferable at low frequencies. Time-frequency methods that use a

constant time-frequency resolution, such as short-time Fourier transforms [19], are unable to appropriately resolve all frequencies.

Another important consideration when performing time-frequency analysis using discrete data points is determining which frequencies can be included. When data points are taken at constant intervals, the highest frequency that can be reliably resolved is half of the sampling frequency [20]. This maximum resolvable frequency is called the Nyquist frequency. Signals oscillating at frequencies that exceed the Nyquist frequency may be interpreted incorrectly if the sampling frequency is lower than the Nyquist frequency. This would result in aliasing and misinterpretation of the signal.

II.2 Wavelet Transforms

There are many methods of performing time-frequency analyses. One such method is the continuous wavelet transform (CWT). CWT is a form of multiresolution analysis, meaning that it analyzes signals at different resolutions depending on their frequencies. It gives better frequency resolution at low frequencies and better time resolution at high frequencies. In CWT a wavelet function is applied as a windowing function.

The wavelets are small waves, generally of finite length. They are compact-supported functions beginning at zero and decaying to zero. The time period between these zero values is known as the window size. The window size of a wavelet can be stretched or compressed to give better time or frequency resolution, respectively. This window is shifted throughout the signal to apply the wavelet transform [21]. Figure 1 includes an example of a wavelet that can be used for wavelet transforms – the Gabor wavelet.

In continuous wavelet transforms, the windowing function is applied to a signal using the following equation to find the magnitude (W) of the signal function f at time t:

$$W(a,b) = \frac{1}{\sqrt{a}} \int_{-\infty}^{\infty} f(t) \overline{\psi\left(\frac{t-b}{a}\right)} \, dt \tag{11}$$

where $\overline{\psi(t)}$ is the complex conjugate of the analyzing wavelet $\psi(t)$, b determines the time the window is localized around, and a is a scaling coefficient that determines the

"size" of the window and is greater than zero. The analyzing wavelet must satisfy the admissibility condition

$$\int_{-\infty}^{\infty} \frac{|\hat{\psi}(\omega)|^2}{|\omega|} d\omega < \infty \tag{12}$$

where ω is the frequency (in radians per second) and $\hat{\psi}(\omega)$ is the Fourier transform of $\psi(t)$ [22]. This Fourier transform is used to convert a signal from the time domain to the frequency domain and can be calculated using the following equation:

$$\hat{\psi}(\omega) = \int_{-\infty}^{\infty} \psi(t) e^{-i\omega t} dt \tag{13}$$

II.3 The Gabor Wavelet Transform

The Gabor wavelet is used for power density calculations because it allows for the resolution in the time and frequency domains to be optimized with minimal uncertainty [22] from the Uncertainty Principle. It is expressed using the following equation:

$$\psi(t) = \frac{1}{\sqrt[4]{\pi}} \frac{\sqrt{\omega_0}}{\gamma} \exp\left[\frac{-\left(\frac{\omega_0}{\gamma}\right)^2}{2} t^2\right] \exp(i\omega_0 t) \tag{14}$$

where γ and ω_0 are positive constants. The Gabor wavelet (left) and its Fourier transform (right) with $\gamma = \pi\sqrt{2/\ln(2)}$ and $\omega_0 = 2\pi$ are shown in Figure 1:

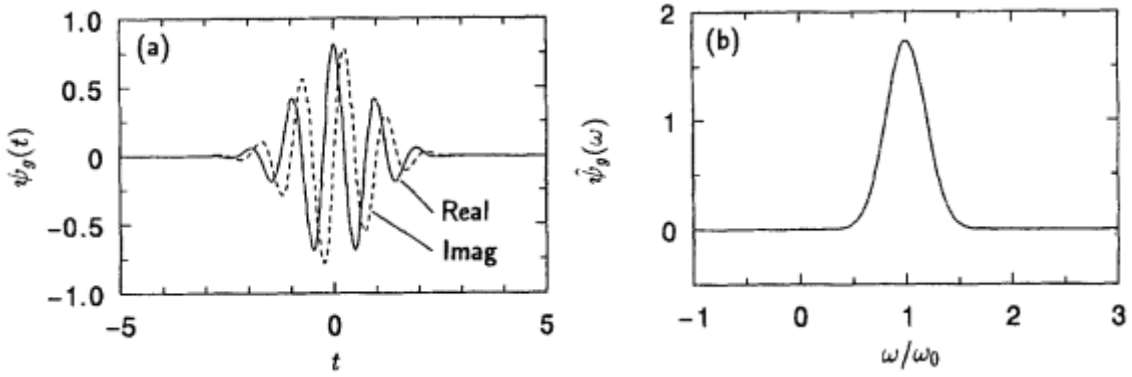

Figure 1: Gabor Wavelet and Its Fourier Transform [22]

The Gabor wavelet is localized around the time $t = b$ and frequency $\omega = \frac{\omega_0}{a}$ (in radians per second). The discrete Gabor wavelet transform uses the following equation to find the magnitude (W) of a function f at a single time and frequency:

$$W(a,b) = \frac{1}{\sqrt{a}} \sum_{k=0}^{N-1} f[kT] \overline{\Psi\left(\frac{\mathrm{kT-b}}{\mathrm{a}}\right)} T \tag{15}$$

where k is the time iteration being analyzed, N is the total number of times being analyzed, and T is the sampling period. The complex conjugate of the Gabor wavelet ($\overline{\Psi}$) at this time and frequency is

$$\overline{\Psi\left(\frac{\mathrm{kT-b}}{\mathrm{a}}\right)} = \frac{1}{\sqrt[4]{\pi}} \frac{\sqrt{\omega_0}}{\gamma} \exp\left[\frac{-\left(\frac{\omega_0}{\gamma}\right)^2}{2} \left(\frac{kT-b}{a}\right)^2\right] \cos\left[\omega_0 \left(\frac{kT-b}{a}\right)\right] \tag{16}$$

Equations 15 and 16 can be repeated for the a and b values corresponding to each time and frequency under consideration. It is important to note that the magnitude of W has no absolute significance on its own. It is a relative term that gives the likelihood of each frequency contributing to the signal at each time. However, the relative magnitudes of W can be used to compare contributions between frequencies.

The time period between data points must be constant when performing Gabor wavelet transforms. The frequencies (ω, in radians per second) that should be used are given by

$$\omega = \frac{2\pi n}{NT}, \quad where\ n = 0, 1, 2, \ldots \tag{17}$$

When samples are taken at discrete intervals, the highest frequency that can be resolved is the Nyquist frequency. A sample signal and its Gabor wavelet transform are given in Figure 2:

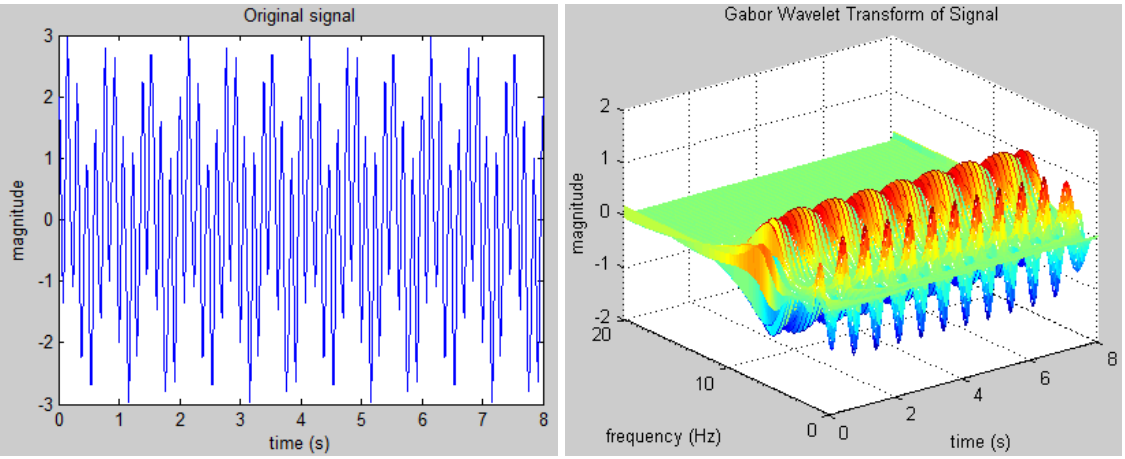

Figure 2: Gabor Wavelet Transform of a Sample Signal

CHAPTER III
THE POWER DENSITY THEORY

III.1 Power Density Theory

The power density theory is a macroscopic method of determining when a material subjected to alternating stresses is likely to fail by fatigue. It is based on the concept that changes in stress deposit power into a volume. These time gradients of stress can occur over a broad bandwidth of frequencies simultaneously. The changes in stress due to each frequency must be considered in fatigue calculations. Higher frequencies cause faster changes in stress, which inflicts more damage than lower frequencies. It is only by considering how much of the change in stress is due to each frequency at each time and then placing more significance on higher-frequency stress alternations that fatigue failure can be fully captured.

Power density (*PD*) is defined as the amount of power deposited into a volume. It is calculated as the time variation of a stress σ as follows:

$$PD = \frac{d\sigma}{dt} = \lim_{\Delta t \to 0} \frac{\Delta\sigma}{\Delta t} = \lim_{\Delta t \to 0} \Delta\sigma \cdot f \tag{18}$$

where *t* is time and *f* is the frequency of the stress alternations. The normal and shear stresses in all directions must be considered. Power density's metric units can be derived as

$$\frac{Pa}{s} \equiv \frac{N}{m^2 \cdot s} \equiv \frac{N \cdot \left(\frac{m}{s}\right)}{m^3} \equiv \frac{W}{m^3} \tag{19}$$

III.2 Power Density Calculations

At a given time while a specimen is undergoing loading and unloading, its stresses oscillate at different amplitudes over a range of frequencies simultaneously. At each frequency, the power density causes damage to the material. High-frequency stress alternations cause more damage than low-frequency alternations. Therefore, it is necessary to separate the changes in stress by the frequencies at which they occur. A broad bandwidth of frequencies must be considered.

Under cyclic loading, there is a change in stress in each of six directions at any given location and time interval. Using a Cartesian coordinate system, these can be labeled as $\Delta\sigma_{xx}$, $\Delta\sigma_{yy}$, $\Delta\sigma_{zz}$, $\Delta\tau_{xy}$, $\Delta\tau_{yz}$, and $\Delta\tau_{zx}$. The changes in stress in every direction must each be transformed into the time-frequency domain separately. The Gabor wavelet transform can be used to accomplish this.

For the purposes of power density calculations, the function *f* from Equation 15 is the change of stress in time in a single direction, such as $\Delta\sigma_{xx}$. Applying Equation 15 to the change in normal stress in the x-direction gives the following equation:

$$W_{xx}(a,b) = \frac{1}{\sqrt{a}}\sum_{k=0}^{N-1}\Delta\sigma_{xx}[kT]\overline{\Psi\left(\frac{\mathrm{kT-b}}{\mathrm{a}}\right)}T \tag{20}$$

where the Gabor wavelet transform magnitude in the normal x-direction is denoted as W_{xx}. The complex conjugate of the Gabor wavelet ($\overline{\Psi}$) can be calculated using Equation 16. Equation 20 gives W_{xx} as a function of *a* and *b*. These two variables can be converted into the times (*t'*) and frequencies (*f'*, in Hz) at which they occur using the following equations:

$$t' = b \tag{21}$$

$$f' = \frac{\omega_0}{2\pi a} \tag{22}$$

This allows W_{xx} to be given as a function of *t'* and *f'*.

In a given time interval, the sum of the changes in x-direction normal stress at each frequency ($\Delta\sigma'_{xx}$) must equal the total change in x-direction normal stress ($\Delta\sigma_{xx}$). This means that the relative magnitudes at each frequency and time interval (W_{xx}) can be scaled to determine the change in stress at that frequency and time interval using the following equation:

$$\Delta\sigma'_{xx}(t',f') = W_{xx}(t',f')\cdot\frac{\Delta\sigma_{xx}(t')}{\sum_{f=0}^{\infty}W_{xx}(t',f)} \tag{23}$$

Equations 20-23 can be repeated for each of the remaining directions of changes in stress. Thus, the changes in stress in each direction at each time interval and frequency ($\Delta\sigma'_{xx}$, $\Delta\sigma'_{yy}$, $\Delta\sigma'_{zz}$, $\Delta\tau'_{xy}$, $\Delta\tau'_{yz}$, $\Delta\tau'_{zx}$) are now known (with the uncertainty inherent in the Gabor wavelet transform time-frequency analysis).

Power density is non-directional even though it takes into account the stresses in all directions. This necessitates a method of resolving the change in stress tensor into a single scalar stress value. This value must be independent of the coordinate system used in determining the stress components.

The method used to achieve this involves first finding the eigenvalues of the *A* matrix, where *A* is the matrix of change in stress tensors at each given time *t'* and frequency *f'*:

$$\mathrm{A} = \begin{bmatrix} \Delta\sigma'_{xx}(t',f') & \Delta\tau'_{xy}(t',f') & \Delta\tau'_{zx}(t',f') \\ \Delta\tau'_{xy}(t',f') & \Delta\sigma'_{yy}(t',f') & \Delta\tau'_{yz}(t',f') \\ \Delta\tau'_{zx}(t',f') & \Delta\tau'_{yz}(t',f') & \Delta\sigma'_{zz}(t',f') \end{bmatrix} \tag{24}$$

The three eigenvalues of *A* are then labelled $\Delta\sigma'_{eig1}$, $\Delta\sigma'_{eig2}$, $\Delta\sigma'_{eig3}$. The resolved magnitude for the change in stress at time *t'* and frequency *f'*, denoted as $\Delta\sigma'$, can be calculated as follows:

$$\Delta\sigma'(t',f') = \sqrt{\left[\Delta\sigma'_{eig1}(t',f')\right]^2 + \left[\Delta\sigma'_{eig2}(t',f')\right]^2 + \left[\Delta\sigma'_{eig3}(t',f')\right]^2} \tag{25}$$

The change in stress tensors must not be resolved into their scalar magnitudes until after the Gabor wavelet transform is applied. Otherwise, the solution would not correctly account for changes in stress in different directions. Some frequencies may be cancelled out while others could be falsely increased.

The resolved magnitude for the change in stress ($\Delta\sigma'$) is used to determine the power density. The power deposited into a volume results from the volume experiencing this change in stress magnitude in time. At a given time, the change in stress at every frequency contributes to the power density. The power density at time *t'* and frequency *f'* is labeled *PD'* and is the product of the frequency and the change in stress at that frequency:

$$PD'(t',f') = \Delta\sigma'(t',f') \cdot f' \tag{26}$$

The total power density from all frequencies at time *t'* is labeled *PD*. It is calculated by adding the power density contributions from each frequency at that time interval:

$$PD(t') = \sum_{f=0}^{\infty} PD'(t',f) \tag{27}$$

In practice, the highest frequency that can be considered is the Nyquist frequency, which is half the sampling frequency.

The accumulated power damage up to a time (PD_{accum}) is calculated by summing the power densities at every time interval up to time *t'*:

$$PD_{accum}(t') = \sum_{t=0}^{t'} PD(t) \tag{28}$$

This gives the total damage inflicted on the material from the power densities at every frequency and time interval.

Power density accumulation eventually damages the component enough to cause it to fail by fatigue. The material is expected to fail once the accumulated power density reaches a certain point – the "power density threshold ($PD_{threshold}$)". In other terms, a material is expected to fail due to fatigue when the following equation is true:

$$PD_{accum} \geq PD_{threshold} \tag{29}$$

The power density threshold is an inherent material property, similar to tensile strength or fracture toughness. Every material has a defined power density threshold under certain conditions. In general, stiffer materials are likely to fail more quickly due to fatigue, so they would have lower power density thresholds.

Factors such as surface finish, temperature, and manufacturing method may impact how the stress waves propagate through a material, which would affect how long it lasts under alternating stresses. For example, a rough surface would create stress concentrations that may increase the power density the component experiences, causing it to fail sooner.

III.3 Applications for the Power Density Theory

The power density theory could be used during the design process whenever fatigue is a concern. Improved accuracy in fatigue calculations would make fatigue failures easier to predict and avoid. Additionally, less uncertainty would allow for smaller safety factors to be used, increasing efficiency. Designers could better optimize systems around fatigue failure. The theory is especially useful when stress alternations are expected to occur at multiple frequencies and directions. However, even single-

frequency cyclic loading generally creates stress oscillation responses at multiple frequencies.

Another potential application for the power density theory is real-time tracking in systems. The magnitudes and frequencies of stress alternations could be monitored at locations of concern. When the power density at a point approaches the power density threshold, the part could be examined and repaired or replaced.

Power density may also have applications related to other types of failure. For example, sudden impact creates broadband stress waves that propagate through a component. The high-frequency waves would create very high power densities, causing the power density threshold to be reached quickly. This implies that lower stresses would be required to break the component, as is seen in reality.

CHAPTER IV
PREVIOUS MULTIAXIAL VIBRATION FATIGUE TESTING

IV.1 Experiment Setup

A feasibility study was performed to test the validity of the power density theory. This study used computer simulations to replicate physical testing performed by Mršnik, Slavič, and Boltežar [23]. This testing was performed on a specimen made of cast aluminum. The part was designed to encourage a multiaxial, multiple-frequency structural response to the applied loads. It was cut into a "Y" shape with a weight attached to both of its arms. There was a large hole in the center of the sample and another smaller hole beneath that one. The smaller hole was used as a mounting point at which a horizontal force excitation was applied during testing. The base of the specimen was fixed to a shaker that applied vertical kinematic excitation. Accelerometers on each arm were used to measure the system response. A diagram of the Y-sample from Mršnik et al. is shown in Figure 3, and a picture of the test setup is shown in Figure 4:

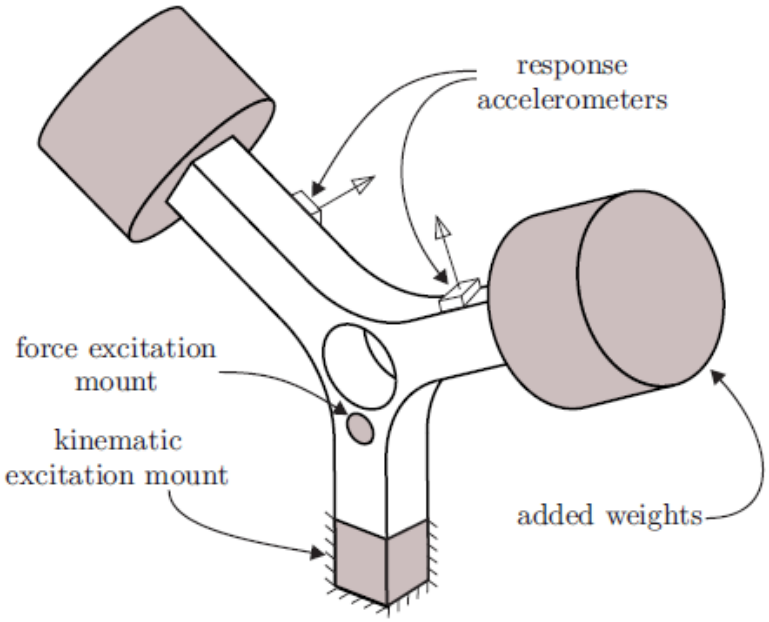

Figure 3: Schematic of the Y-Sample [23]

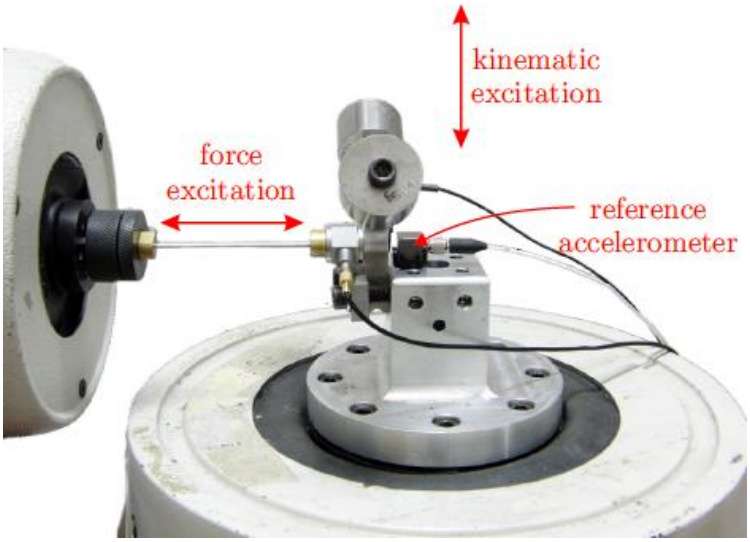

Figure 4: Experimental Setup [23]

The vertical kinematic excitation was applied as a uniform, broadband frequency profile spanning from 380-480 Hz. This range was chosen to include the sample's resonant frequency in the vertical direction. This expedited testing by increasing the stresses experienced by the part. For the horizontal force excitation, a broadband frequency profile spanning from 290-390 Hz was targeted. Again, this range included the resonant frequency mode in the direction of the applied force. According to Mršnik et al., the actual response was not as uniform as was intended. Figure 5 and Figure 6 show the measured frequency responses in the horizontal and vertical directions, as well as the responses of the model created by Mršnik et al.:

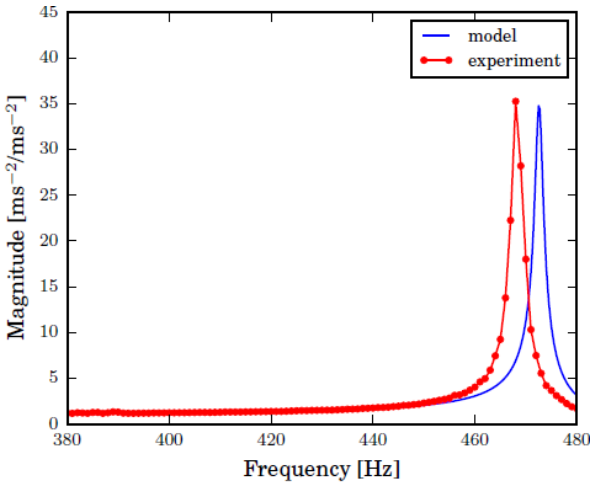

Figure 5: Frequency Response Function in the Direction of Kinematic Excitation [23]

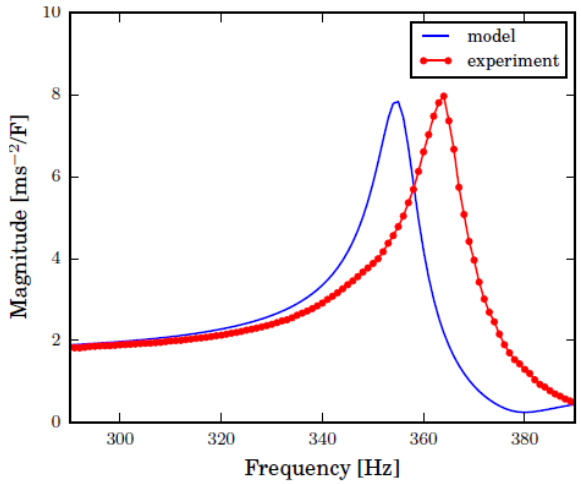

Figure 6: Frequency Response Function in the Direction of Force Excitation [23]

The force and kinematic loads were applied at these frequencies until surface cracking was detected for ten different load cases. The magnitudes of vertical kinematic excitation and horizontal force excitation applied to the system were different for each case. The measured root mean square loads from each case (from Mršnik et al.) are given in Table 1 and Figure 7:

Table 1: Measured Root Mean Square Horizontal Force and Vertical Acceleration Combinations

Load Cases		
Case	F_{rms} (N)	a_{rms} (m/s^2)
1	2.42	12.26
2	2.51	14.81
3	2.32	16.97
4	3.11	8.44
5	3.36	9.71
6	3.36	12.56
7	3.39	14.62
8	3.94	7.85
9	4.06	10.79
10	3.73	12.46

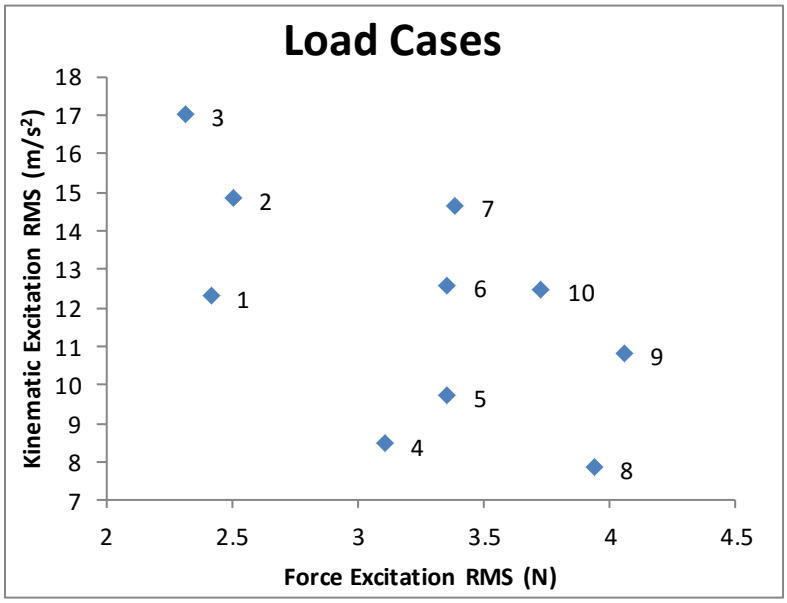

Figure 7: Measured Root Mean Square Horizontal Force and Vertical Acceleration Combinations

IV.2 Previous Fatigue Failure Prediction

Mršnik et al. predicted the fatigue lifetime and failure location for each case using the Tovo-Benasciutti method [8,10,23], a numerical fatigue method in the frequency domain. The power spectral density (PSD), denoted at $S(\omega)$, was used to give

the stress intensity in the frequency domain. The moments m_i of the PSD were calculated using

$$m_i = \int_{-\infty}^{\infty} \omega^i S(\omega) d\omega \tag{30}$$

where ω is the frequency in radians per second. These moments can be used to find the expected positive crossings rate ν_0^+, expected peak rate ν, and spectral width parameters α_i using the following equations:

$$\nu_0^+ = \frac{1}{2\pi}\sqrt{\frac{m_2}{m_0}} \tag{31}$$

$$\nu = \frac{1}{2\pi}\sqrt{\frac{m_4}{m_2}} \tag{32}$$

$$\alpha_i = \frac{m_i}{\sqrt{m_0 m_{2i}}} \tag{33}$$

The Tovo-Benasciutti damage intensity ($\bar{D}^{TB}$) was then calculated using the following equation:

$$\bar{D}^{TB} = [b + (1-b)\alpha_2^{k-1}]\alpha_2 \bar{D}^{NB} \tag{34}$$

where the numerically-determined constant (b) and narrow-band damage intensity ($\bar{D}^{NB}$) were found as follows:

$$b = \frac{(\alpha_1-\alpha_2)[1.112(1+\alpha_1\alpha_2-(\alpha_1+\alpha_2))e^{2.11\alpha_2}+(\alpha_1-\alpha_2)]}{(\alpha_2-1)^2} \tag{35}$$

$$\bar{D}^{NB} = \nu_0^2 C^{-1}\left(\sqrt{2m_0}\right)^k \Gamma\left(1+\frac{k}{2}\right) \tag{36}$$

The fatigue strength curve from the stress-life method was used to predict the fatigue lifetime of the material. Equation 1 was rearranged to the following form to determine constants C and k:

$$C = N\left[\left(S_f'\right)_N\right]^k \tag{37}$$

Both C and k were chosen based on the best fit of the numerical results to the experimental results and applied to all ten load cases.

These equations are based on uniaxial stress alternations. However, stresses occur in every direction in this experiment. To make these equations usable, six different multiaxial methods [23] were attempted to reduce the stress tensor to a single equivalent stress value: maximum normal stress [24], maximum shear stress [24], maximum normal

and shear stress [24], Preumont and Piéfort [25], Carpinteri-Spagnoli criterion [26], and the Projection-to-Projection approach [27]. The predictions using each of these methods were compared to the experimental results.

IV.3 Test Results

The experimental failure times were between 20 and 135 minutes. Mršnik et al. did not explicitly report the experimental fatigue lifetimes for each case except in comparison to their theoretical predictions. They found that the six multiaxial methods typically predicted similar fatigue lifetimes. However, their lifetime predictions sometimes deviated from their experimental results by 200% or more. Figure 8 compares the fatigue lifetimes projected using the maximum shear stress theory with the experimental results. The dashed line represents a 200% deviation, and the dotted line represents a 300% deviation.

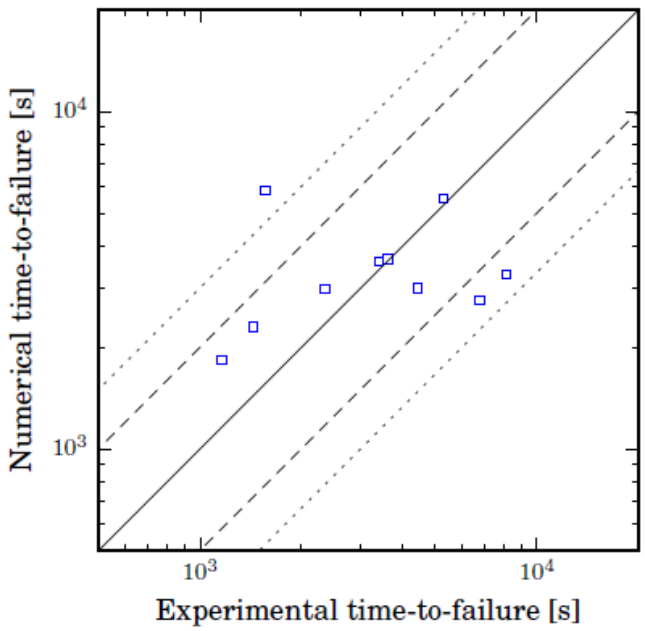

Figure 8: Previously Predicted Fatigue Lifetimes versus Experimental Results [23]

The results of these experiments showed that the failure location varied depending on the ratio of the force excitation magnitude to the kinematic excitation magnitude. More force-dominant excitations tended to result in cracks as much as 3.3 mm lower than acceleration-dominant cases. The failure locations in Figure 9 were given in order of increasing force-dominance:

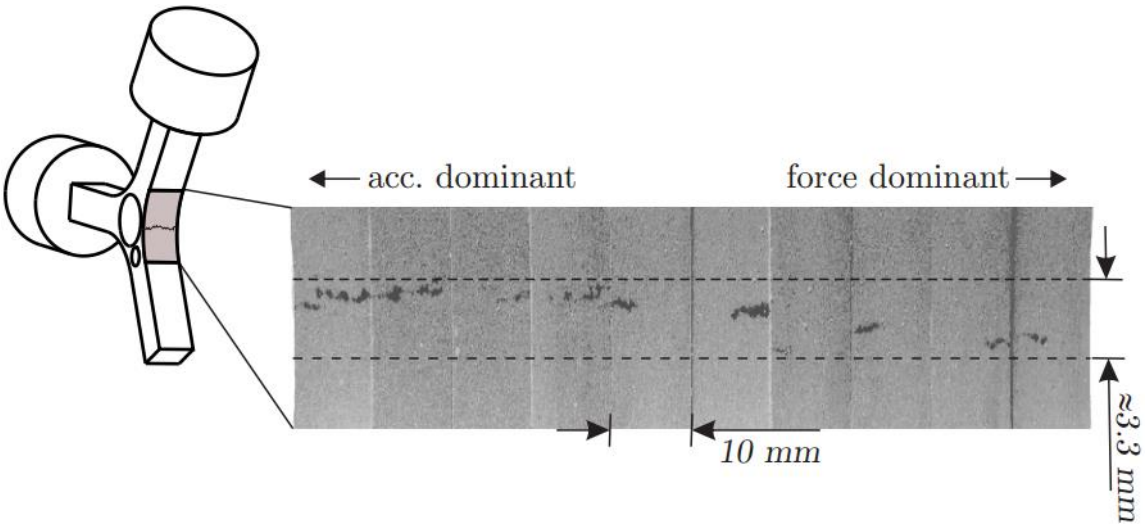

Figure 9: Failure Locations for Each Case [23]

For each case, the six multiaxial criteria always predicted approximately the same failure location. For more acceleration-dominant cases, they predicted that the cracking would occur on the outside of the sample, near the actual failure location (point C_2 on Figure 10). After a certain level of force-dominance was reached in a case, the predicted failure location jumped to a location inside the center hole (point C_1 on Figure 10). This is different from the experimental results for the force-dominant cases, which showed cracking on the outside edge, a little below where acceleration-dominant cases failed. Figure 10 shows the time-to-failure contour and critical points predicted by Mršnik et al. for a force-dominant case (left) and an acceleration-dominant case (right):

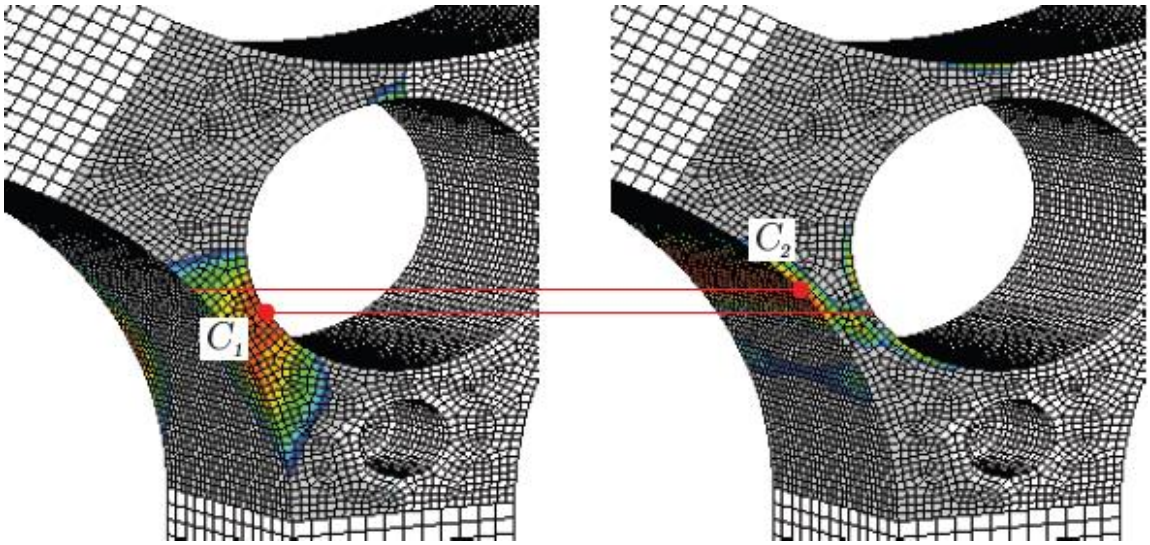

Figure 10: Previously Predicted Failure Locations for Force- and Acceleration-Dominant Cases [22]

CHAPTER V
POWER DENSITY FEASIBILITY STUDY METHODOLOGY

V.1 Computer Simulations

A computer model of this experiment was built in Abaqus to test the feasibility of the power density method. Mršnik, Slavič, and Boltežar did not report some of the dimensions of the sample they tested. The unknown dimensions were estimated using the images they presented of their test setup and finite element model mesh. Pictures of the test setup were favored when accounting for any discrepancies between them and the mesh. Figure 11 gives the dimensions of the Abaqus model generated for the thesis work:

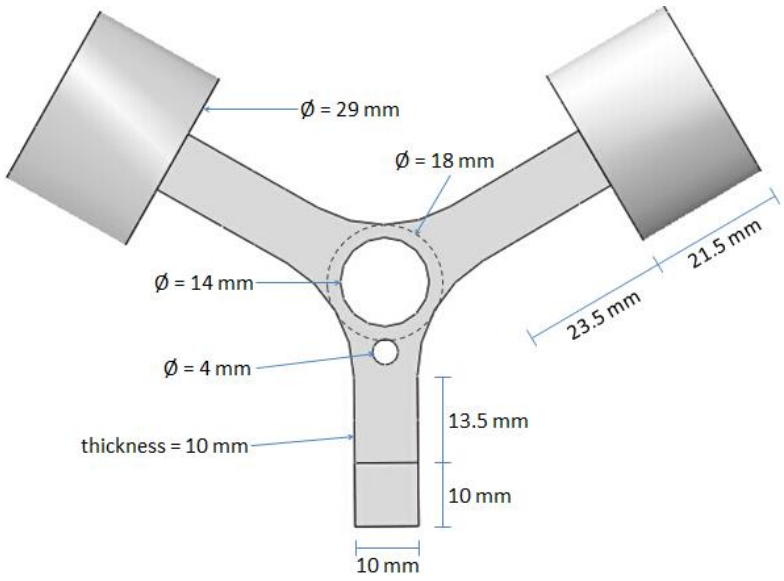

Figure 11: Abaqus Model Dimensions

The material of the actual Y-sample was AlSi7Cu3. Complete properties for this material are not available, though. Therefore, the material properties of AlCuMg1 were used in this model. This same assumption was made by Mršnik, Slavič, and Boltežar.

The model was meshed with explicit three-dimensional stress elements, allowing for nonlinearity and transient loads to be well-captured. Hex elements were used so the part would have freedom to deform in all directions. For explicit analysis in Abaqus, hex elements must be of a linear geometric order, but second-order accuracy was placed on the calculations. Nodes were placed approximately 0.4 mm apart near the middle of the sample where the stress waves were of most concern. The mesh gradually became coarser near the ends. A convergence study (Figure 22 in the Appendix) was performed to ensure that this element size was proper. The Abaqus mesh used for these simulations is shown in Figure 12:

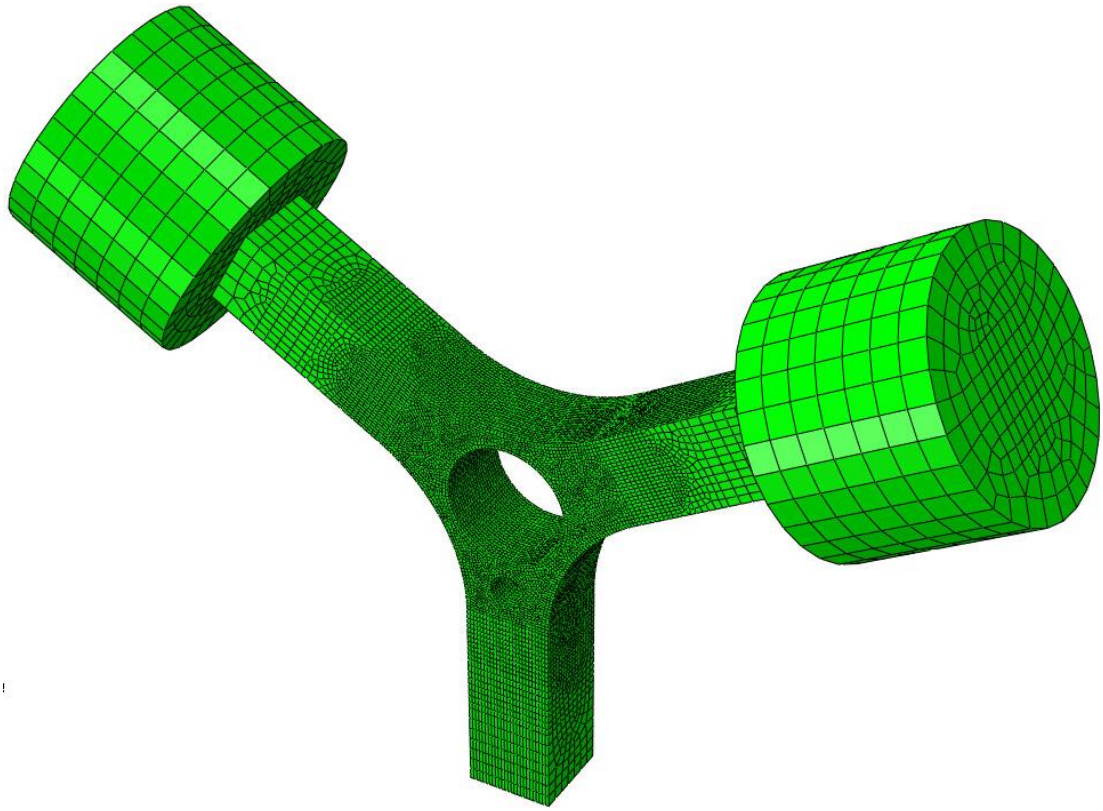

Figure 12: Y-Sample Mesh

Kinematic excitation was applied vertically to the front and back faces on the bottom 10 mm of the model. It was assumed to be sinusoidal with a frequency of 465

Hz, the peak frequency found in the vertical direction of the physical tests (Figure 5). The excitation amplitude varied for each case such that the root mean square of the acceleration matched the values given in Table 1. These faces were also constrained to allow zero displacement in any other direction. A horizontal surface traction was applied to the lower hole. This excitation was assumed to be a 365 Hz sinusoidal wave, which was the peak frequency found in the horizontal direction of the physical tests (Figure 6). Attempting to recreate the random broadband frequencies would add too much complexity and computation time for the purposes of this feasibility study. The traction amplitude for each case created a root mean square force on the area that corresponded with the values given in Table 1. Additionally, standard gravity was assumed in the vertical direction for the whole part at all times.

Running the simulations to predicted failure would have been impractical. A shorter time span could still be used for this feasibility study to determine which cases accumulated power density the fastest. Therefore, Abaqus/Explicit was used to run the simulations for 0.301 seconds, resulting in about 140 kinematic excitation cycles and about 110 force excitation cycles. This was long enough for the system to reach a steady power density accumulation pattern. The stresses were output every $1x10^{-5}$ seconds. This high sampling rate produced a large amount of data. Stresses could only be taken on the surface where cracking was observed (highlighted in Figure 9) due to computational memory limitations. Only one of the two sides needed to be examined due to symmetry.

V.2 Power Density Calculations

The results of the Abaqus simulations were post-processed using MATLAB. The MATLAB program used the simulations' stress outputs to determine the power density accumulation of each element on this surface. These calculations were performed as described in the Power Density Theory section.

The Gabor wavelet constant ω_0 was defined as 2π so that $1/a$ would equal the frequency in Hz. The constant γ was set to equal $\pi\sqrt{2/\ln(2)} = 5.336$ per Goupillaud, Grossmann, and Morlet [28]. If the change in stress over a time interval (such as $\Delta\sigma_{xx}$)

was very small, any imprecision in Gabor transform magnitudes (such as W_{xx}) would be magnified when that value was scaled using Equation 23. This resulted in falsely high or low $\Delta\sigma'_{xx}$ values. Therefore, the median scale factor across all time intervals was used to transform W_{xx} to $\Delta\sigma'_{xx}$. This was done for each element and stress direction separately. Scaling in this manner eliminated false extreme scaling and kept the results consistent for every time interval.

At the beginning of the simulations, high frequency responses created high power densities. These responses faded quickly, and the power density accumulation stabilized. Only data from the 0.269-0.301 seconds time span was used. This avoided the initial high-frequency oscillations. The power density accumulation during this time span would be expected to continue until the sample cracked. This 0.032 seconds interval was long enough to capture about 15 kinematic excitation cycles and about 12 force excitation cycles while maintaining a reasonable computation volume. Very close to the beginning and end of this interval, the Gabor wavelet transform could not accurately determine how much each frequency contributed to the stress alternations. To circumvent this issue, results from the first and last 0.001 seconds of the time span were not considered. All of the presented results occurred between 0.27 seconds and 0.30 seconds. This allowed the power density accumulation for each case to be reliably compared.

The highest frequency that could be resolved was limited by the sampling frequency. The power densities from frequencies higher than 50,000 Hz could not be determined in these simulations. For the purposes of this feasibility study, comparisons were performed neglecting differences in very high-frequency power densities among elements. A faster sampling rate would increase the required computational resources, but it would be necessary to resolve higher frequencies.

CHAPTER VI
POWER DENSITY VALIDATION RESULTS

VI.1 Simulation Failure Locations

The power densities experienced by each element were compared for all ten load cases. The locations that accumulated the most power density over the measured time interval would be expected to fail first due to fatigue. Figure 13 shows the crack locations for each case, sorted from most acceleration-dominant to most force-dominant. It also shows the predicted power density accumulation at each location. Red indicates high accumulation, and blue indicates low accumulation. Elements that are darker red are predicted to have a higher probability of cracking first. The element with the highest predicted power density accumulation is highlighted as a yellow box. Because the experimental crack location images are pictures of a curved surface, the exact positions do not perfectly line up with the predicted power density accumulation at that location.

Two locations emerged as having the highest power density accumulation, one on the upper half of the examined surface and one on the lower half. The force-dominant cases (Cases 4, 5, 8, 9, and 10) were predicted to have a higher probability of failing low than the acceleration-dominant cases (Cases 1, 2, 3, 6, and 7). This trend is in line with the experimental results and is a promising indication for the validity of the power density theory.

The kinematic excitation caused the Y-sample's arms to raise and lower, creating bending stresses that were highest at the examined surface. Inspection of the system showed that the kinematic excitation alone tended to cause the largest stress magnitudes at the height where acceleration-dominant cases failed. It also caused relatively large stresses at the height where force-dominant cases failed, although these magnitudes were significantly lower than at the upper location. At all heights, the kinematic excitation induced higher power densities near the middle than at the edges.

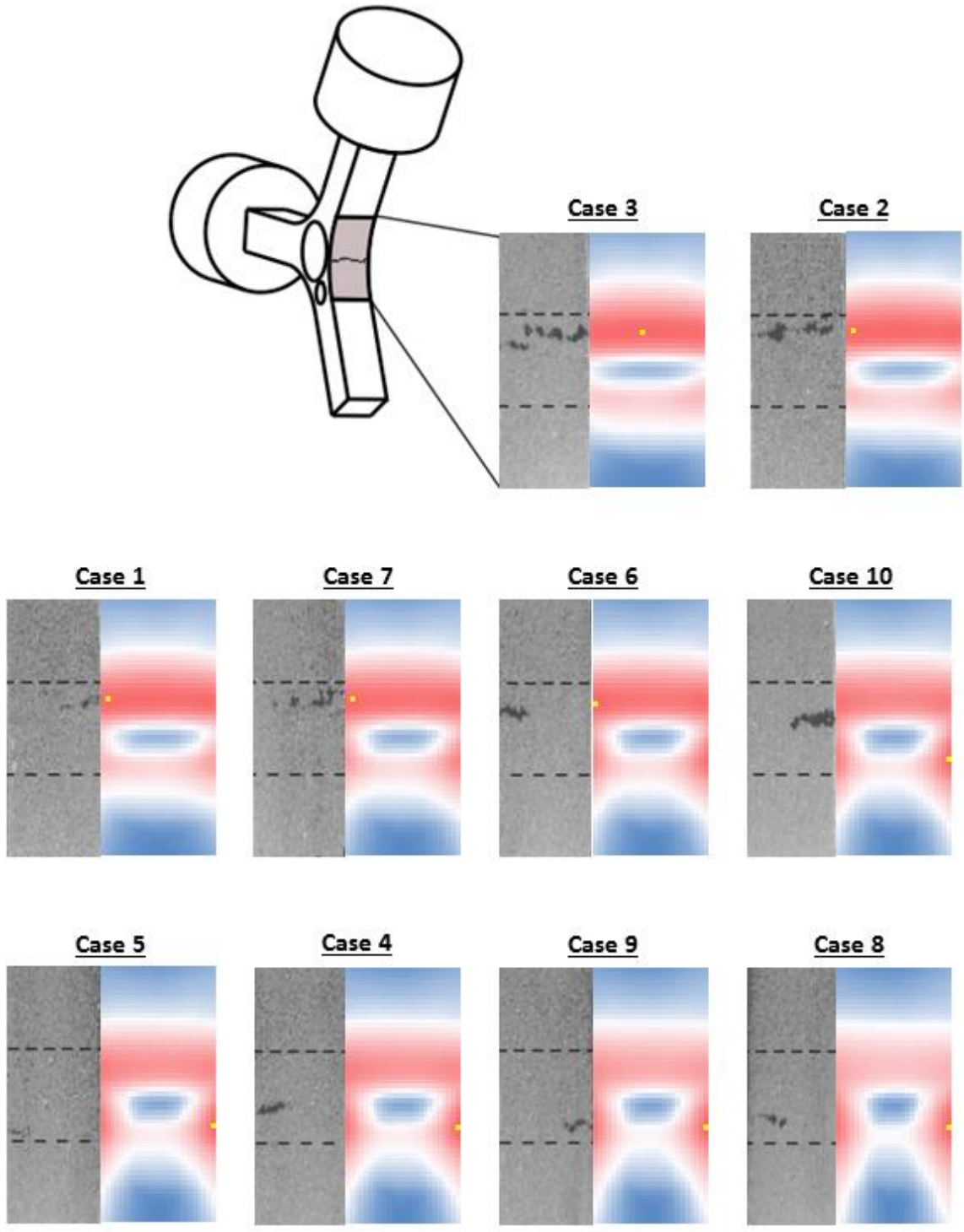

Figure 13: Experimental Versus Predicted Failure Locations for Each Case

The force excitation created bending about a different axis, causing the sample to sway in the direction of the applied force. This produced high stresses on the edges of the examined surface, especially on the lower half. As the level of force-dominance was increased, the power densities near the edges increased as well.

An extremely acceleration-dominant case would be projected to fail on the upper half of the examined surface, near the middle. As force-dominance (and the associated power densities near the edges) increases, the predicted failure location moves towards the edge. Then, at a certain level of force-dominance – between that of Case 6 and Case 10 – the predicted failure location switches from the upper portion to the lower portion. The power densities near the edges of the lower portion are mainly caused by the force excitation while the power densities in the upper portion are mainly caused by the kinematic excitation. At a level of force-dominance between that of Case 6 and Case 10, the force excitation creates a high enough power density difference between the lower portion and the upper portion to overcome the difference caused by kinematic excitation.

The most force-dominant case, Case 8, was predicted to fail 5.2 mm lower than the most acceleration-dominant case, Case 3. This margin is wider than the 3.3 mm difference observed in the testing. This may be due to the finite element model having slightly different dimensions from the actual Y-sample since the exact dimensions were not given by Mršnik et al. Also, it was not clear whether the reported 3.3 mm difference was measured linearly or circumferentially along the curved edge. If Mršnik et al. measured linearly, the experimental difference would be closer to the difference found by the Abaqus simulations, which were measured circumferentially.

The predicted failure locations of some cases – especially Case 10 – differed from the test results slightly. This is also likely a result of slight inaccuracies in the model's dimensions. It was found that small changes in the model's dimensions could affect the level of force-dominance at which the predicted failure location switched from the top half to the bottom half. Additionally, the predicted power density accumulation assumes that all elements have the same properties. Any inconsistencies in the real

sample – such as surface imperfections – could affect where it actually fails. In every case, the part cracked at a location that was predicted to have a high probability of failure.

VI.2 Simulation Fatigue Lifetimes

Table 2 gives the power density (in gigawatts per cubic meter) accumulated between 0.27-0.30 seconds by the critical element of each case. Without knowing the power density threshold for this material, fatigue lifetimes can only be estimated relative to each other. Additionally, since Mršnik et al. did not report the failure times for each case, the lifetimes predicted using power density cannot be compared with their results.

Table 2: Power Density Accumulation of the Critical Elements

Highest Power Density Accumulation			
Case	F_{rms} (N)	a_{rms} (m/s^2)	PD_{acc} (GW/m^3)
1	2.42	12.26	582.45
2	2.51	14.81	660.47
3	2.32	16.97	726.53
4	3.11	8.44	536.60
5	3.36	9.71	581.62
6	3.36	12.56	617.11
7	3.39	14.62	676.78
8	3.94	7.85	676.00
9	4.06	10.79	700.65
10	3.73	12.46	652.85

The critical elements with higher power density accumulation are predicted to fail more quickly. Therefore, Case 3 is expected to fail first, and Case 4 is expected to last the longest. Force excitation and kinematic excitation both affected the predicted fatigue life.

Among acceleration-dominant cases, higher forces resulted in higher power densities. This can be seen by comparing Case 2 with Case 7. Both cases were acceleration-dominant and were predicted to fail at the same location. Case 7 had a lower acceleration than Case 2 but a higher force. The increased force resulted in faster power density accumulation for Case 7 than Case 2. Similarly, acceleration magnitude affected the power density accumulation in force-dominant cases, although to a slightly lesser degree. Higher accelerations caused power density to accumulate faster.

VI.3 Power Density Response

The power density response at the critical element for each case was analyzed. There was a notable difference between the critical elements of the acceleration-dominant cases (on the upper half of the examined surface) and those of the force-dominant cases (on the lower half of the examined surface). The responses were similar among acceleration-dominant cases, with the main difference being the magnitudes of the stresses and power densities. The same was true among force-dominant cases.

Figure 14 shows the resolved changes in stress ($\Delta\sigma'$) experienced by the critical element of Case 1 – an acceleration-dominant case – from 0.27-0.30 seconds. Figure 15 shows the resulting power density contributions by each frequency at each time (PD'):

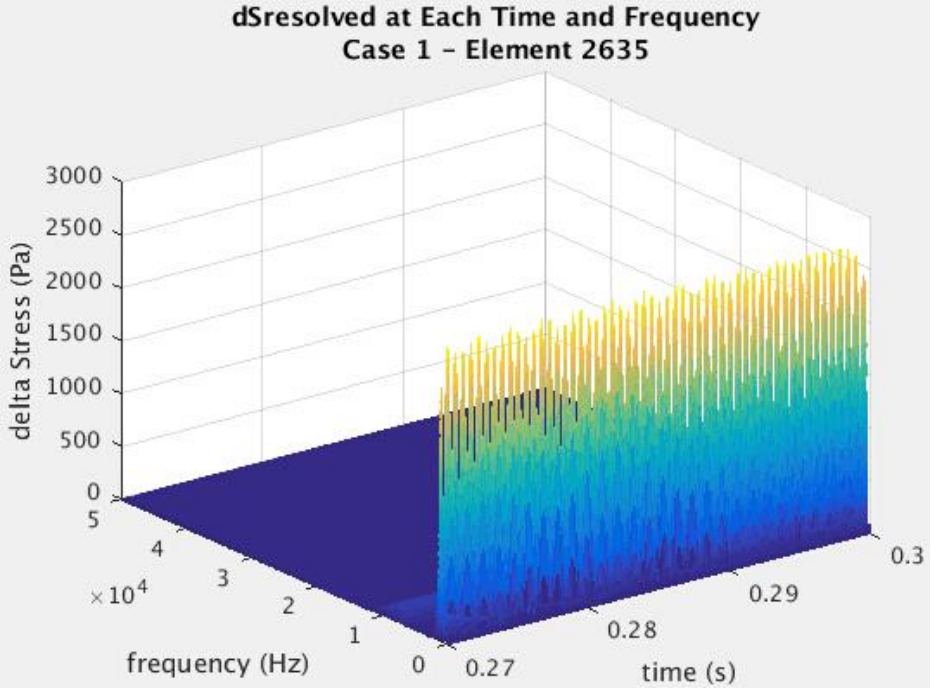

Figure 14: Resolved Change in Stress Magnitudes for the Critical Element of Case 1

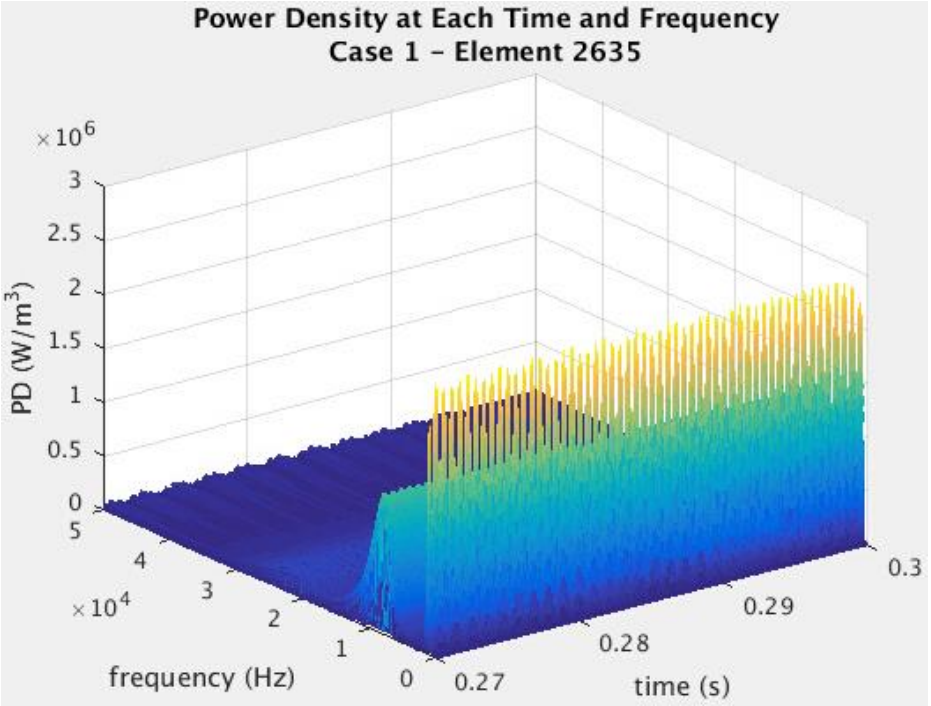

Figure 15: Power Densities Due to Each Frequency at Each Time for the Critical Element of Case 1

The biggest changes in stress were at low frequencies, close to those of the applied excitations. However, because power density is weighted by frequency, higher frequencies contributed significantly to the power density of each element. Power density peaks can be seen around the excitation frequencies as well as at approximately 9,000 Hz. The power density response was consistent throughout this time period.

The power densities at each frequency combined to give the total power densities at each time (*PD*) shown in Figure 16. The figure only includes 0.28-0.29 seconds so that more detail can be seen, but the power densities were similar for the rest of the time period.

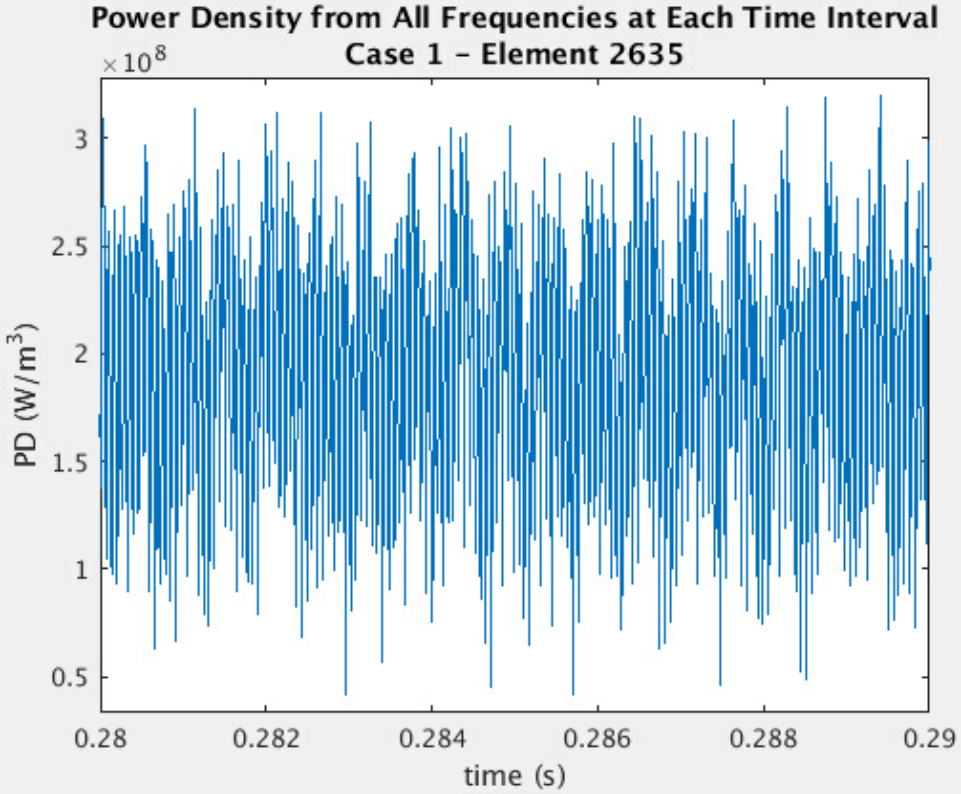

Figure 16: Total Power Densities at Each Time for the Critical Element of Case 1

These power density oscillations accumulated over time to form a nearly linear trend. This accumulation between 0.27 seconds and 0.30 seconds is shown in Figure 17.

The values shown for power density accumulation (PD_{acc}) start at zero. In reality, power density had accumulated prior to this time. However, only the accumulation during this time period (after the stress alternations had stabilized) was considered so that initial high-frequency stresses did not affect comparisons between elements.

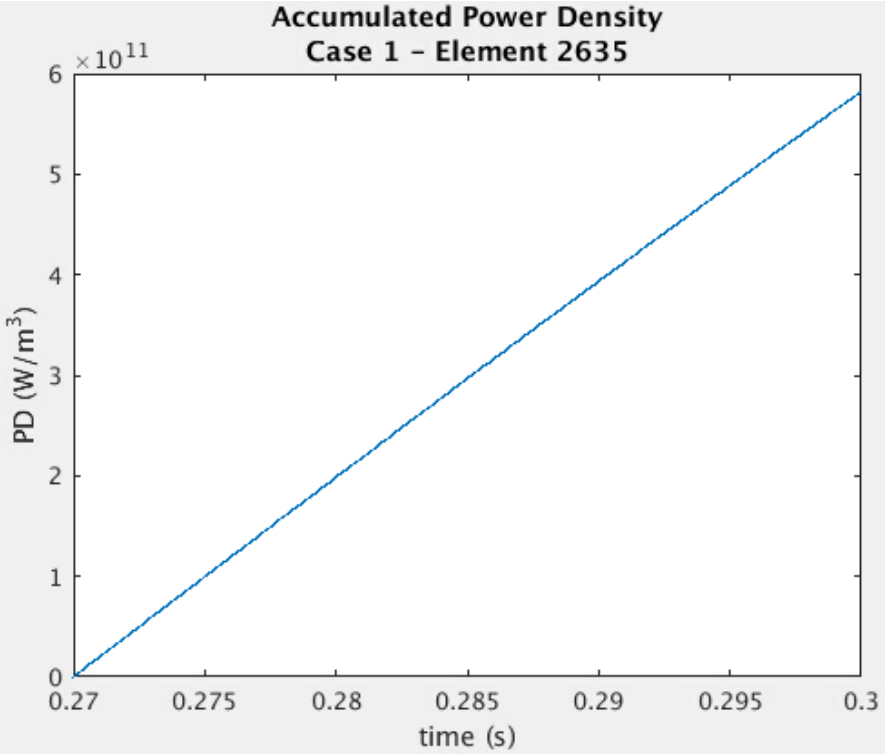

Figure 17: Power Density Accumulation at the Critical Element of Case 1

Figure 18 through Figure 21 show how the power density accumulated between 0.27 seconds and 0.30 seconds in Case 4, which was force-dominant. Other force-dominant cases gave similar results.

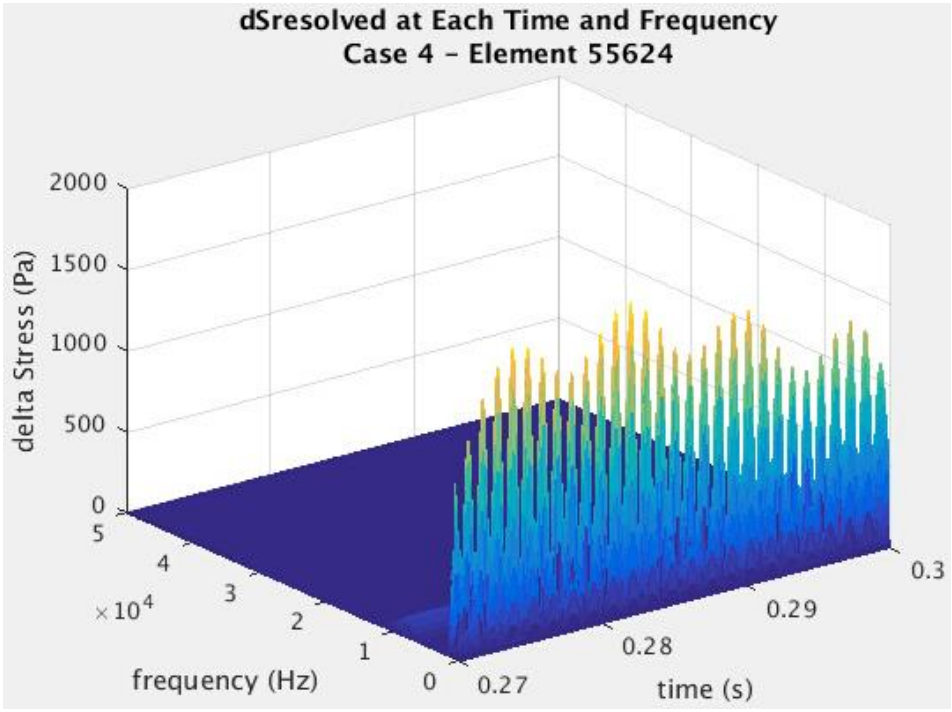

Figure 18: Resolved Change in Stress Magnitudes for the Critical Element of Case 4

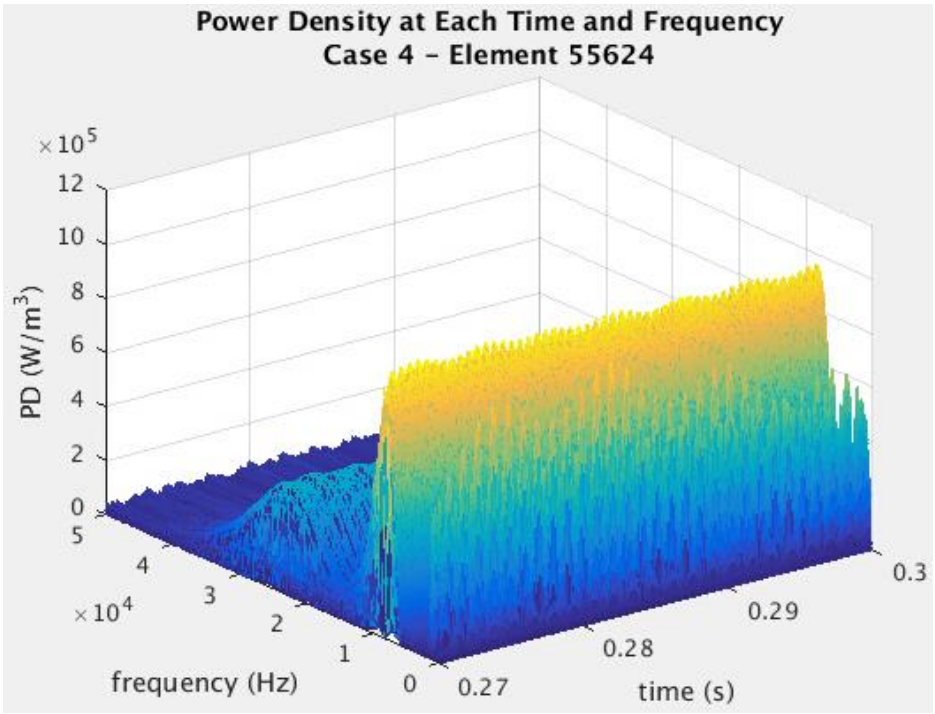

Figure 19: Power Densities Due to Each Frequency at Each Time for the Critical Element of Case 4

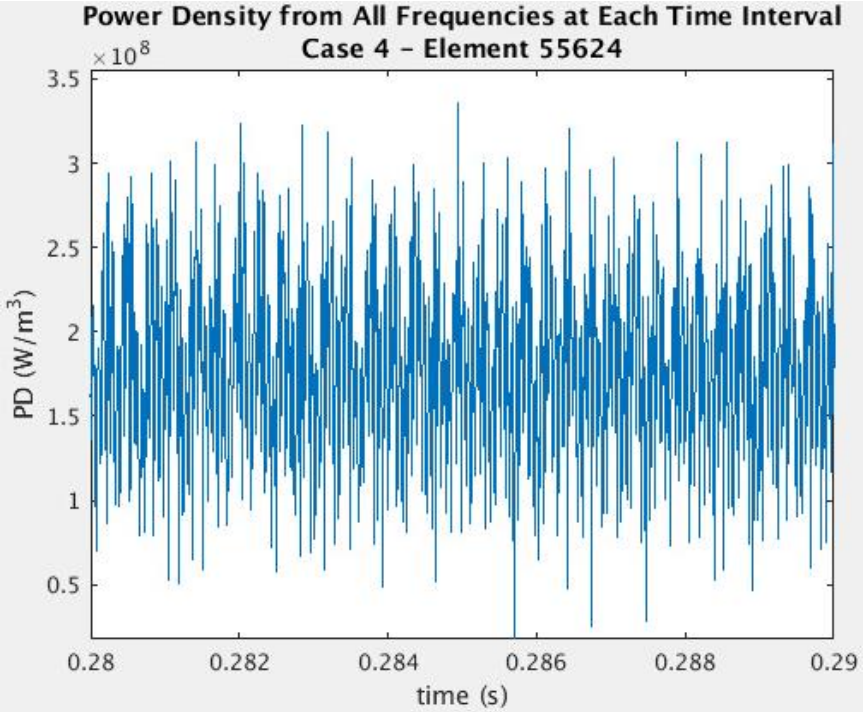

Figure 20: Total Power Densities at Each Time for the Critical Element of Case 4

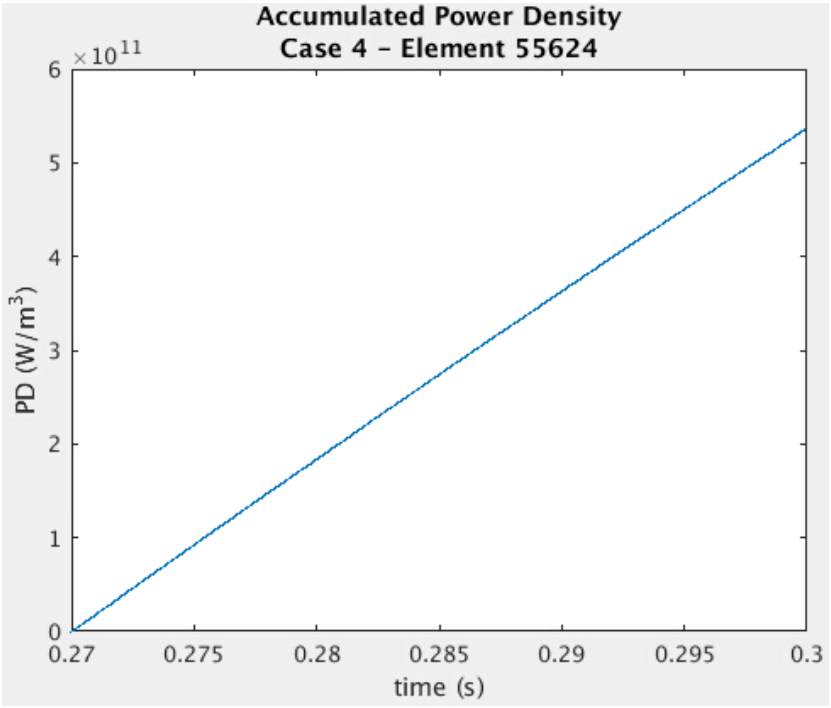

Figure 21: Power Density Accumulation at the Critical Element of Case 4

At the critical elements of the force-dominant cases, there was an additional peak frequency around 25,000 Hz that contributed to the power density. This very high-frequency peak helped contribute enough power density in the force-dominant cases to cause the predicted failure to switch to the lower portion of the examined surface, even if it did not experience quite as high of stresses as the upper portion.

From the simulations, bending in the horizontal direction always occurred at the same frequency as the force excitation. However, bending of the Y-sample's arms up and down due to kinematic excitation happened at almost twice the frequency of the applied acceleration. Small changes in the model were found to affect this frequency. If the inertia of the arms in the model was decreased – by changing the length of the arms or the size of the weights on the end – the bending frequency increased. Similarly, increasing the arm's inertia slowed the bending in the vertical direction. Changes that caused the arm to bend faster resulted in higher power densities per cycle even if they lowered the stresses. This is a difference between the power density theory and most time-domain theories. Time-domain theories estimate that lower stresses would cause less damage, regardless of the frequencies at which they occur.

CHAPTER VII
FUTURE RESEARCH AND CONCLUSIONS

VII.1 Recommended Future Research

The results of this feasibility study indicate that the power density theory may be a viable explanation for fatigue failure. However, more research needs to be done to further validate the theory. This includes physical testing. The feasibility study provides a guideline for developing an experimental plan to establish and confirm that the power density threshold is a fundamental material property. Stress alternations at multiple frequencies could be applied to parts until a fatigue crack forms. While this is occurring, their three-dimensional strains over time could be monitored with a strain gauge. The strains could then be converted into the corresponding stress tensor, and the power density accumulation at the time of failure could be calculated. Under the power density theory, parts of the same material would be expected to fail after approximately the same amount of power density has accumulated (the power density threshold), regardless of the stress magnitudes and frequencies that made up the power density.

A similar process could be used to determine the power density thresholds for various materials. Once the power density thresholds of materials have been determined, power density could be used to predict fatigue lifetimes. Until then, power density can only be used to compare which locations or designs would fail earlier than others. Other details of power density will also need to be examined to further understand it. The ways in which different frequencies and stresses in all directions contribute to the material's power density should be researched. In addition, other applications of power density outside of fatigue, such as impact, should be explored.

VII.2 Conclusions

Current methods of predicting fatigue failure lack a proper scientific basis. They rely on empirically-derived equations and often neglect important factors, such as the frequencies of stress alternations. Although these theories are often useful, they have

high levels of uncertainty and do not provide parameters that are of definitive physical meaning. In contrast, the power density theory is a new way of viewing fatigue failure that is based on the physical phenomenon of power being deposited into a volume during stress oscillations. It quantifies fatigue with two physical parameters, stress variation and the frequency at which it occurs.

The results of the feasibility study showed that the failure locations predicted using power density followed the same trend as the experimental results. This indicates that the power density theory may be a viable alternative for characterizing fatigue failure. In order to further validate and develop this theory, additional research must be performed in the future. The development of a scientific theory that can accurately explain and predict fatigue failure would be enormously beneficial in a wide range of engineering applications. This opportunity to advance our understanding of fatigue should be pursued.

REFERENCES

1. Juvinall, Robert C., and Kurt M. Marshek. *Fundamentals of Machine Component Design*. 5th ed. Hoboken, New Jersey: John Wiley & Sons, 2012. Print.
2. Callister, William D., Jr., and David G. Rethwisch. *Materials Science and Engineering*. 8th ed. Hoboken, New Jersey: John Wiley & Sons, 2011. Print.
3. Budynas, Richard G., and J. Kieth Nisbett. *Shigley's Mechanical Engineering Design*. 9th ed. New York, New York: McGraw-Hill, 2011. Print.
4. Arutyunyan, R. A. "Frequency Dependence of the Fatigue Strength Criterion." *Strength of Materials* 17.12 (1985): 1717-720. *SpringerLink*. Web. 8 June 2016.
5. Makhlouf, Kamel, and J.W. Jones. "Effects of Temperature and Frequency on Fatigue Crack Growth in 18% Cr Ferritic Stainless Steel." *International Journal of Fatigue* 15.3 (1993): 163-71. *ScienceDirect*. Web. 8 June 2016.
6. Stinchcomb, W. W., K. L. Reifsnider, and R. S. Williams. "Critical Factors for Frequency-dependent Fatigue Processes in Composite Materials." *Experimental Mechanics* 16.9 (1976): 343-48. *SpringerLink*. Web. 8 June 2016.
7. Holmes, John W., Xin Wu, and Bent F. Sørensen. "Frequency Dependence of Fatigue Life and Internal Heating of a Fiber-Reinforced/Ceramic-Matrix Composite." *Journal of the American Ceramic Society* 77.12 (1994): 3284-286. *Wiley Online Library*. John Wiley & Sons, Inc. Web. 8 June 2016.
8. Mršnik, Matjaž, Janko Slavič, and Miha Boltežar. "Frequency-domain Methods for a Vibration-fatigue-life Estimation – Application to Real Data." *International Journal of Fatigue* 47 (2013): 8-17. *ScienceDirect*. Web. 8 June 2016.
9. Dirlik, Turan. *Application of Computers in Fatigue Analysis*. Diss. U of Warwick, 1985. *University of Warwick Publications Service & WRAP*. Web. 8 June 2016.
10. Benasciutti, D., and R. Tovo. "Spectral Methods for Lifetime Prediction under Wideband Stationary Random Processes." *International Journal of Fatigue* 27.8 (2005): 867-77. *ScienceDirect*. Web. 8 June 2016.
11. Abdullah, S., M. Z. Nuawi, C. K. E. Nizwan, A. Zaharim, and Z. M. Nopiah. "Fatigue Life Assessment Using Signal Processing Techniques." Proc. of 7th WSEAS International Conference on Signal Processing, Robotics and Automation, University of Cambridge, Cambridge, England. N.p.: n.p., 2008. 221-25. Web. 9 June 2016.
12. Ricker, Dennis W. *Echo Signal Processing*. Norwell, Massachusetts: Kluwer Academic, 2003. Web. 9 June 2016.
13. Cooley, James W., Peter A. W. Lewis, and Peter D. Welch. "The Fast Fourier Transform and Its Applications." *IEEE Transactions on Education* 12.1 (1969): 27-34. *IEEE Xplore*. Web. 9 June 2016.

14. Logan, Daryl L. *A First Course in the Finite Element Method*. 5th ed. Boston, Massachusetts: Cengage Learning, 2012. Print.

15. "Overview of ABAQUS/Explicit." *IMechanica*. Harvard School of Engineering and Applied Sciences, n.d. Web. 11 June 2016.

16. "Abaqus 6.13 Documentation." Dassault Systèmes, n.d. Web. 9 June 2016.

17. Boashash, Boualem, ed. *Time-Frequency Signal Analysis and Processing: A Comprehensive Reference*. 2nd ed. London, England: Academic, 2016. Web. 7 June 2016.

18. Folland, Gabor, D. "Theory of Communication. Part 1: The Analysis of Information." *The Journal of the Institution of Electrical Engineers - Part III: Radio and Communication Engineering* 93.26 (1946): 429-41. *IEEE Xplore*. Web. 9 June 2016.

19. Jacobsen, E., and R. Lyons. "The Sliding DFT." *IEEE Signal Processing Magazine* Mar. 2003: 74-80. *IEEE Xplore*. Web. 7 June 2016.

20. Oppenheim, Alan V., Ronald W. Schafer, and John R. Buck. *Discrete-Time Signal Processing*. 2nd ed. Upper Saddle River, New Jersey: Prentice Hall, 1999. Print. Prentice-Hall Signal Processing Ser.

21. Polikar, Robi. *The Wavelet Tutorial, Second Edition*. University of Nevada, Reno, n.d. Web. 8 June 2016.

22. Inoue, H., K. Kishimoto, and T. Shibuya. "Experimental Wavelet Analysis of Flexural Waves in Beams." *Experimental Mechanics* 36.3 (1996): 212-17. Print.

23. Mršnik, Matjaž, Janko Slavič, and Miha Boltežar. "Multiaxial Vibration Fatigue — A Theoretical and Experimental Comparison." Mechanical *Systems and Signal Processing* 76-77 (2016): 409-23. *ScienceDirect*. Web. 12 Feb. 2016.

24. Nieslony, Adam, and Ewald Macha. *Spectral Method in Multiaxial Random Fatigue*. New York City, New York: Springer, 2007. Web. 9 June 2016.

25. Pitoiset, X., and A. Preumont. "Spectral Methods for Multiaxial Random Fatigue Analysis of Metallic Structures." *International Journal of Fatigue* 22.7 (2000): 541-50. *ScienceDirect*. Web. 9 June 2016.

26. Carpinteri, Andrea, Andrea Spagnoli, and Sabrina Vantadori. "Reformulation in the Frequency Domain of a Critical Plane-based Multiaxial Fatigue Criterion." *International Journal of Fatigue* 67 (2014): 55-61. *ScienceDirect*. Web. 9 June 2016.

27. Cristofori, A., D. Benasciutti, and R. Tovo. "A Stress Invariant Based Spectral Method to Estimate Fatigue Life under Multiaxial Random Loading." *International Journal of Fatigue* 33.7 (2011): 887-99. *ScienceDirect*. Web. 9 June 2016.

28. Goupillaud, P., A. Grossmann, and J. Morlet. "Cycle-octave and Related Transforms in Seismic Signal Analysis." *Geoexploration* 23.1 (1984): 85-102. *ScienceDirect*. Web. 30 Apr. 2016.

APPENDIX

Convergence Study

Figure 22 shows the results of the convergence study. This was performed on Case 6, which is in between the most force-dominant and acceleration-dominant cases. The maximum deflection was determined based on the application of the most extreme forces applied to the sample. The feasibility study was performed using 95,095 elements.

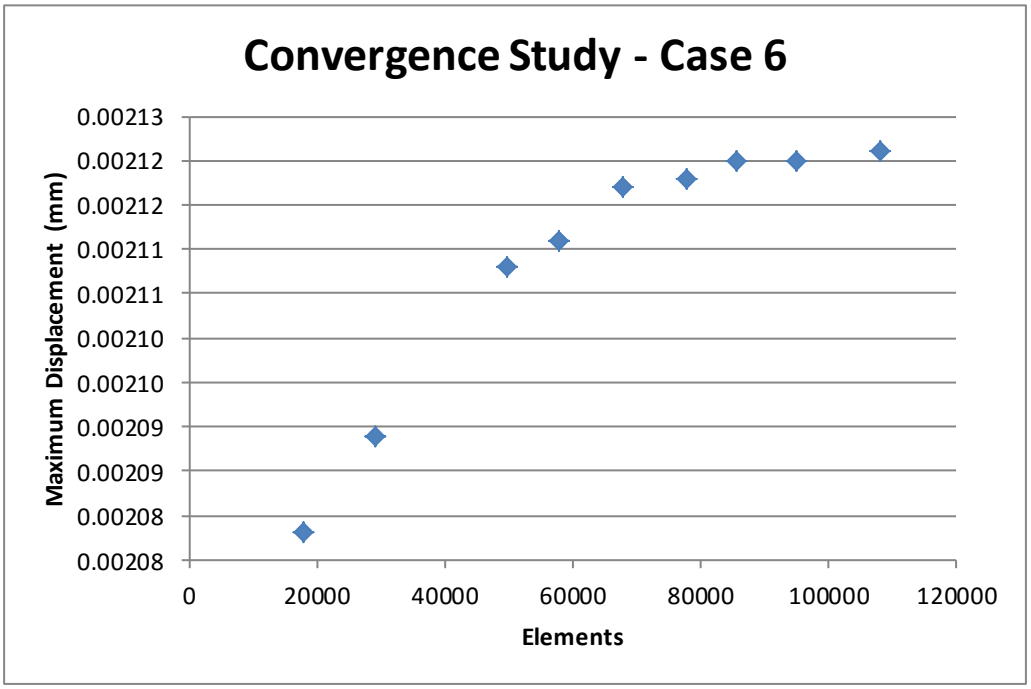

Figure 22: Convergence Study